Molecular Ordering and 2D Conductivity in Ultrathin Poly(3-hexylthiophene)/Gold Nanoparticle Composite Films

Virginia Ruiz,[†] **Patrick G. Nicholson,**[†] **Stuart Jollands,**[‡] **Pamela A. Thomas,**[‡]
Julie V. Macpherson,[†] **and Patrick R. Unwin*,**[†]

Departments of Chemistry and Physics, University of Warwick, Coventry CV4 7AL, U.K.

Received: July 4, 2005; In Final Form: August 11, 2005

This paper reports the first comparison of the structure and electrical conductivity properties of spin cast (SC) and Langmuir−Schaeffer (LS) films of regioregular poly(3-hexylthiophene) (P3HT). In addition, the effect of incorporating highly monodisperse Au nanoparticles (NPs), with a core diameter of ∼5 nm, into SC and LS P3HT films is described. A detailed picture of molecular organization in the films has been obtained using ultraviolet−visible absorption spectroscopy, atomic force microscopy, field-emission scanning electron microscopy, X-ray diffraction, and X-ray reflectivity. Film morphology was correlated with pseudo-two-dimensional conductivity measured using scanning electrochemical microscopy, with P3HT in the semiconducting regime. It was found that SC films, which were slightly thicker than those formed with the LS technique, exhibited greater organization. This resulted in an order of magnitude higher lateral conductivity for the SC films. Inclusion of Au NPs (50 wt %) into both SC and LS films resulted in the formation of uniform and relatively flat (rms roughness ∼1 nm) composite films. Surprisingly, the addition of NPs did not disrupt the characteristic crystal structure found for the native P3HT films. The effect of Au NPs on film lateral conductivity was found to be determined by the distribution of Au NPs within the polymer, which varied significantly between SC and LS films. Whereas Au NPs aggregated into hexagonally packed clusters in SC films, NPs in LS films were predominantly uniformly distributed between the lamella bilayer. It was found that, while the inclusion of Au NPs caused the lateral conductivity to decrease in SC films, in LS films, the lateral conductivity increased by a factor of 2.

Introduction

Elucidating the electrical properties of nanosized materials is currently of great interest, particularly with regard to developing "bottom-up" approaches for engineering nanoelectronic devices.[1−3] Metallic nanoparticles (NPs) offer unique electronic, optical, and catalytic properties[4] which have seen applications in catalysis, sensors, and biomedical and nanoelectronic devices.[5,6] To organize NPs into controlled and functional assemblies, different types of linkers have been used, including dithiols, polyelectrolytes, and inorganic ions.[7−11] NPs have also been embedded into polymer matrixes to produce nanocomposites that combine the properties of the host polymer and guest NP.[12,13] In particular, π-conjugated polymers (CPs) have been found to act as promising scaffolds for NPs, resulting in materials which have applications in electrocatalysis,[14−16] chemical sensors,[17,18] electrochemical capacitors,[19] and protective coatings against corrosion.[20] An advantage of using CPs as linkers in metal NP assemblies, apart from the evident flexibility and processability of the ensemble, is the possibility of tuning the conductivity of the material after assembly by chemically or electrochemically doping the polymer.[21]

CPs are of great interest in their own right because their mechanical, optical, and electrical properties are attractive for the development of a new generation of organic light emitting diodes, photovoltaic devices, and organic field effect transistors (OFETs). Among CPs, the family of regioregular poly(3-

alkylthiophenes) (P3ATs) has shown the most promise for OFET applications, with regioregular poly(3-hexylthiophene) (P3HT, the focus of this paper) exhibiting the highest mobility among P3ATs.[22] The OFET mobility of injected charge carriers in regioregular P3HT is 2−3 orders of magnitude higher than regiorandom P3HT and approaches the values found in amorphous silicon.[23] The fast charge transport in regioregular P3HT films has been rationalized by reference to the structural characteristics of the polymer. P3HT self-assembles in the solid state into a lamellar-type bilayer with strong cofacial π−π interchain plane stacking.[24] The high level of intra- and interchain order has led to recent revision of the nature of polaronic and excitonic species in P3HT: only singly charged polaronic charge carriers exist, and both polarons and excitons cannot be considered to be confined to a single chain but rather have a strong interchain nature.[24−26]

Although intensely studied, the mechanism of charge transport in CPs is far from being completely understood. A plethora of models including fluctuation induced hopping,[27] granular rod,[28] and random resistor network[29] have been used to explain charge transport in CPs in the metallic regime. For P3HT, the model of charging-energy-limited tunneling between conducting islands has been successfully applied.[31] In addition, Mott's law of variable-range hopping[30] has been used successfully to describe charge transport in P3HT in the semiconducting regime.[31,32]

CP/NP composites can be prepared in a variety of ways, including electrochemical deposition of nanoparticles onto electrodes previously coated with a CP,[14−16] photochemical preparation,[33,34] reduction of metal salts dissolved in a polymer

* Corresponding author. E-mail: p.r.unwin@warwick.ac.uk.
† Department of Chemistry.
‡ Department of Physics.

matrix,[35-37] polymerization of the CP around nanoparticles,[38,39] and solution mixing of nanoparticles into a polymer matrix.[40] Production of nanocomposites from solution mixtures is advantageous in that each component can be purified and size-selected prior to blending and the amount of each component can be precisely controlled.

Spin casting is suitable for forming films of compounds that are soluble in low boiling point solvents and has been used to produce thin films of P3HT in which lamella crystalline regions have been found, as determined by X-ray diffraction (XRD).[24,41] The Langmuir−Blodgett (LB) technique has also been employed to fabricate thin films of P3HT. However, due to the lack of a strong polar group to interact with the aqueous side of the air/water interface, P3HT has usually been mixed with common amphiphiles such as arachidic acid[42] or stearic acid[43] to produce ordered LB films, but these have inferior mobilities with respect to spin cast (SC) films of pure P3HT. Several authors have reported[44,45] that pure P3HT LB films cannot be made and that spreading P3HT onto water results in the formation of polymeric islands. However, a recent study states that contiguous Langmuir (probably bilayer) films of pure P3HT can be transferred to a solid support using the Langmuir−Schaeffer (LS) (horizontal dipping) technique[46] and we have adapted this latter protocol to produce LS films for the present work.

Since the conductivity of P3HT can be tuned over 7 orders of magnitude (10^{-4}−10^3 S/cm) by the degree of doping,[47] it was important to carefully select the doping level of the polymer to best investigate the influence of the Au NPs on the conductivity of P3HT. Thus, the polymer was studied in its unintentionally doped form, that is, doped solely by exposure to air. In electrical terms, this means that the polymer is deep in the semiconducting side of the semiconducting-to-metallic transition. For OFET applications, the study of charge transport in CPs across the semiconducting to metallic states, especially in just one or a few monolayers, that is, within the expected thickness of the channel accumulation layer,[48] is of paramount importance.

Scanning electrochemical microscopy (SECM) has recently been shown to be a sensitive probe of lateral chemical and charge transport processes in thin films, including LS films of metal NPs[49-51] and metal NP/polyelectrolyte hybrid films.[52] A growing body of applications spans charge injection and lateral charge transport in polyaniline monolayers and multilayers,[53,54] redox polymers,[55] and the lateral diffusion of protons[56,57] and redox-active amphiphiles.[58] In addition to its sensitivity, SECM is a noninvasive (noncontact) method capable of precisely applying a spatially localized (a few tens of micrometers) perturbation to an interface. Moreover, SECM does not require the film to be externally biased, and as the film is assembled on an inert substrate, the measured response is solely due to the film without any contribution of the substrate. For these reasons, SECM was chosen to investigate film conductivity in the present work.

This paper presents a detailed analysis of the morphology, molecular structure, and charge transport properties of ultrathin, pseudo-2D, regioregular P3HT films prepared by the SC and LS methods. Further, the morphological, structural, and electrical effects of incorporating Au NPs into the P3HT matrix are investigated. The studies herein provide an understanding of how molecular organization and charge transport are intimately linked for both CPs and CP/NP composites.

Experimental Section

Chemicals. All chemicals were of the highest commercially available purity and were used as received. Regioregular poly-(3-hexylthiophene-2,5-diyl) was purchased from Aldrich (synthesized via the Rieke route,[59] with >98.5% head-to-tail couplings, $M_w \approx 87\,000$ g mol^{-1}) and kept and weighed in a glovebox under a nitrogen atmosphere. All aqueous solutions were prepared from doubly distilled Milli-Q reagent water (Millipore Corp.) with a resistivity ≥ 18 MΩ cm at 25 °C.

Preparation of Dodecanethiolate-Protected Gold Particles. Au NPs (1.6 nm core diameter) were synthesized using the two-phase Brust method[60] and thermally annealed using the method reported by Shimizu et al.[61] to yield NPs with an average core diameter of 5.4 ± 0 3 nm, as determined from transmission electron microscopy (TEM) images of drop cast films on carbon-coated copper grids.[62]

Film Formation. To compare the results obtained from the two different P3HT film preparation procedures, uniform SC and LS films of comparable thickness were prepared. This necessitated the use of different concentrations of P3HT in the starting solution (SC, 1 mg mL^{-1}; LS, 0.1 mg mL^{-1}).

Preparation of SC Films. Polished borosilicate microscope glass slides (BDH, UK) were cut into ~1 cm^2 squares and cleaned in piranha solution. *CAUTION: This reacts violently with organics and should be handled with extreme caution!* They were then sonicated for 5 min each in acetone, propan-2-ol, and cyclohexane and finally blown dry with filtered nitrogen. Films were formed by spin casting chloroform solutions of P3HT (1 mg mL^{-1}) and 1:1 w/w P3HT/Au NP blends. Henceforth, 1:1 specifies the weight ratio. Lower concentrations resulted in the formation of patchy, discontinuous films. Film roughness and uniformity were found to be very sensitive to composition ratio.[62] For the NP composites, a ratio of 50 wt % was chosen, as this resulted in relatively flat (rms roughness ~1 nm) uniform films. Note that, in these films, a 1:1 composition corresponds to a molar ratio of 6×10^3 P3HT monomer/1 Au NP. Spin casting was achieved using a Cookson Electronics, SCS, G3-8 spin coater (U.S.A.) at a ramping speed of 0.1 s, a spin speed of 800 rpm, and a spin time of 40 s. Films were subsequently annealed by heating at 90 °C for 5 min on a heating plate and then stored under a dry nitrogen atmosphere in a glovebox prior to characterization.

Preparation of LS Films. Clean glass slides (vide supra) were rendered hydrophobic (essential for LS deposition) by immersion in a 5% solution of hexamethyldisilozane (Lancaster) in acetone for 30 min. They were then rinsed well with toluene to remove unreacted silane and dried at 110 °C in an oven for 20 min. P3HT and 1:1 blends of P3HT/Au NP were spread from chloroform solutions onto a pure water (Milli-Q, Millipore) subphase in a poly(tetrafluoroethylene) (PTFE) Langmuir trough which had a maximum area of 170 cm^2 (NIMA Instruments, Coventry, U.K.). Spreading chloroform solutions of concentrations above 0.2 mg mL^{-1} led to the formation of aggregates at the air/water interface; hence, all Langmuir films were made from 0.1 mg mL^{-1} P3HT chloroform solutions. The Langmuir trough was housed in a clean room under a laminar flow hood, and air flow was turned off when isothermic compression commenced. Chloroform was allowed to evaporate for at least 1 h prior to compression (long evaporation times resulted in the most consistent isotherms). In all cases, the compression rate was 10 cm^2 min^{-1}. Langmuir films were compressed to the desired surface pressure (35 mN m^{-1}) and held at that pressure until no significant movement of the barriers was required to keep the pressure stable. P3HT and 1:1 P3HT/Au NP films were then transferred horizontally onto a silanized glass slide, by bringing down a dipper to touch the monolayer for a few seconds, before subsequently lifting the glass substrate.

P3HT/Au NP Composite Films

J. Phys. Chem. B, Vol. 109, No. 41, 2005 **19337**

The monolayers were annealed by heating at 90 °C for 5 min and stored under a dry nitrogen atmosphere in a glovebox prior to characterization.

Field-Emission Scanning Electron Microscopy (FE-SEM). FE-SEM images were taken with a Zeiss Supra 55 VP (U.S.A.) instrument. SC and LS samples were mounted onto glass and onto silanized highly n-doped (Sb) Si substrates (Silicon Sense, Inc., U.K.), respectively. Si substrates were cleaned and silanized in a manner analogous to the glass substrates and were used to minimize charging effects during imaging.

Tapping-Mode Atomic Force Microscopy (TM-AFM). TM-AFM images were taken in air with a Digital Instruments multimode atomic force microscope with a Nanoscope IIIa controller (Veeco, U.S.A.).

Ultraviolet−Visible (UV−vis) Absorption Spectroscopy. UV−vis absorption spectroscopy was measured with a Lambda 25 UV−vis spectrometer (Perkin-Elmer Instruments).

X-ray Characterization. Two X-ray techniques were used: diffraction (utilizing Bragg reflection geometry) and specular reflectometry. A Panalytical X'Pert Pro MRD laboratory X-ray source was used at the Cu Kα wavelength ($\lambda = 1.540\,56$ Å). The incident beam optics comprised a hybrid 4 bounce Ge [220] monochromator/mirror unit with a 1/8th beam divergence slit, the choice of which was determined by sample parameters. To minimize background noise, a parallel plate collimator was employed in the diffracted beam path (defining an acceptance angle of 0.27°). In the case of reflectometry, an additional 0.1 mm receiving slit was also used to further restrict the diffracted beam and increase the resolution at grazing angles of incidence. X-ray photons were counted using a gas proportional detector. The experiments were conducted as previously described in detail elsewhere.[63]

Note that although spin casting produces very uniform films in the center of the substrate, thickness tends to increase radially toward the edge of the sample. In the standard configuration,[63] reflectometry measurements probe relatively large areas (approximately several square millimeters) and the effect of this macroscopic thickness variation was to cause suppression of the Kiessig fringes. Accordingly, SC samples were measured using a 1/32nd incidence divergence slit corresponding to a limited 2 mm illuminated sample length so that Kiessig fringes were visible. For data analysis, the X'Pert Reflectivity package from Panalytical was employed which utilizes the Fresnel equations in conjunction with Parratt's recursive formula.[64] This divides the sample into thin layers of uniform electron density for simulation. A fit to the measured profile is achieved using manual adjustment and a genetic algorithm. While simulation is the most accurate method of determining structure, it should be emphasized that models cannot distinguish between root-mean-square (rms) roughness at the boundary between two regions of uniform density and a larger region of material with a density gradient; they both have the same effect of suppressing the Kiessig fringes and are both modeled as thin layers of uniform density.[65,66] The parameters of the system (layer thickness, density, and roughness) were allowed to vary within physically reasonable values to obtain the closest fit (as determined by the absolute square root of the difference), resulting in estimates for the layer thickness, mass density, and rms roughness at the interfaces.

Scanning Electrochemical Microscopy (SECM). Measurements were performed using a simple home-built instrument consisting of a manual x, y, z stage (M-431, Newport Corp., CA) and a z-axis piezoelectric positioner and controller (models P-843.30 and E-501.00, Physik Instrumente, Waldbronn, Ger-
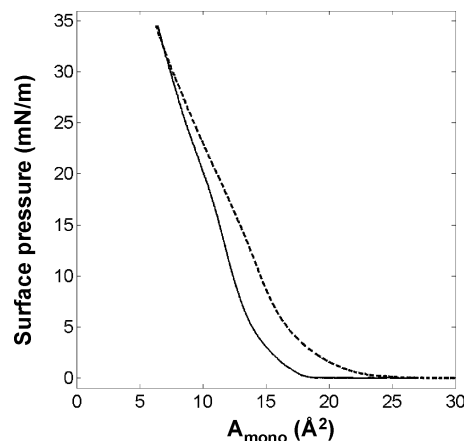

Figure 1. Compression isotherms for P3HT (—) and P3HT/Au NP composite films (- - -). Surface pressure (Π) is plotted versus the mean monomer area (A_{mono}) calculated by taking into account only the mass of the polymer.

many) to give fine control of the ultramicroelectrode (UME) probe in the direction normal to the sample. Cyclic voltammetry and approach curves were recorded using an electrochemical analyzer (CH Instruments, model CHI730A). A two-electrode arrangement was used with a Pt UME as the working electrode and a Ag/AgCl wire acting as a reference electrode. For approach curve measurements, the current from the potentiostat was recorded simultaneously with the UME position directly to a PC using a Lab PC-1200 card (National Instruments, TX) and home-written Quick Basic software. The Pt UME was a 25 μm diameter disk with a glass insulating sheath, characterized by $R_G = 8$ (ratio of the overall tip radius to that of the platinum disk) as determined from both optical micrographs and SECM approach curve experiments to inert substrates followed by fitting.[67] Ferrocenemethanol (Aldrich) and lithium chloride (Aldrich) (concentration typically 0.1 mol dm^{-3}) were used as the redox mediator and base electrolyte, respectively, in all experiments.

Results and Discussion

Films at the Air/Water Interface. P3HT is not an amphiphile and hence not ideally suited to manipulation by the Langmuir technique. However, it was found that good Langmuir films could be made by judicious choice of the concentration of the spreading solution. Figure 1 shows typical surface pressure (Π)/molecular area (A_{mono}) isotherms for P3HT and 1:1 P3HT/Au NP. A_{mono} represents the area per hexylthiophene monomer and was calculated solely on the basis of the mass of P3HT spread. In this way, the effect of adding NPs is readily seen.

The shape of the isotherm of P3HT is comparable to those previously reported.[46,68] At 35 mN m^{-1}, the mean molecular area is ∼6.4 Å^2. This area is approximately half that of a single thiophene unit (14.5 Å^2), estimated for a close-packed monolayer with the thiophene rings standing vertically, with the polymer chains parallel to the air/water interface.[46] Thus, assuming this orientation, the isotherm suggests a bilayer arrangement, at least at relatively high pressures, as shown schematically in Figure 2. A lamella bilayer structure is characteristic of P3ATs[59] and other hairy, rodlike CPs.[69]

The P3HT/Au NP isotherm is slightly shifted to larger molecular areas, notably at low to medium surface pressures, and phase transitions are less marked compared to the P3HT isotherm. As A_{mono} does not take into account the addition of Au NPs, any significant increase in the mean molecular area,

19338 *J. Phys. Chem. B, Vol. 109, No. 41, 2005*
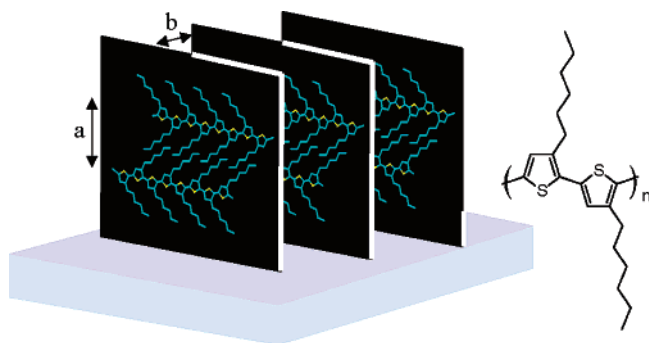
Ruiz et al.

Figure 2. (left) Schematic of the proposed structural orientation of P3HT with respect to the horizontal plane (air/water or solid support). (right) Molecular structure of P3HT.

TABLE 1: Mean Monomer Area (A_{mono}), Film Thickness (Δz), rms Roughness, Conductivity (σ), and Wavelength of the Maximum in the UV−Visible Spectra (λ_{max}) for the Films Studied

	A_{mono} (Å^2)	Δz^a (nm)	rms roughness^a (nm)	σ^b (10^{-4} S cm^{-1})	λ_{max} (nm)
SC P3HT		7	1.16	9.9 ± 0.03	554
LS P3HT	6.4	5	1.26	0.38 ± 0.07	528
SC P3HT/Au NP (1:1)		15	1.03	6.8 ± 0.03	560
LS P3HT/Au NP (1:1)	6.5	10	1.28	0.66 ± 0.04	541

^{a} Determined by TM-AFM. ^{b} Determined by SECM.

compared to P3HT alone, signifies that the NPs cause some separation of the polymer chains parallel to the air/water interface. However, as can be seen in Figure 1, at a transfer pressure of 35 mN m^{-1}, A_{mono} (6.5 Å^2) is similar to P3HT alone, indicating that the NPs are likely to be located either on top or between polymer chains (or both). Since NPs are protected with dodecanethiol chains, a configuration where the NPs avoid the air/water interface is not unexpected. Neither of the isotherms indicated signs of collapse even at high surface pressures of 40 mN m^{-1}.

Film Morphology. *P3HT Films.* Langmuir films were transferred onto hydrophobic glass substrates by the LS method at $\Pi = 35$ mN m^{-1}, corresponding to the liquid condensed region of the isotherm. Optically, films appeared very uniform. For the fabrication of SC films, ramping time, spinning speed, and solution concentration were optimized to produce ultrathin films (i.e., comparable to LS films) that were optically uniform (although some accumulation of material at the sample edges was inevitable). Note that, for the study of SC films, characterization was at or near the center of the films.

Film thickness, topography, roughness, and morphology were probed using TM-AFM and FE-SEM. A summary of thickness and roughness (calculated from representative 5 μm × 5 μm images), along with other parameters, to be discussed later, is presented in Table 1. TM-AFM revealed the surface of all films to be uniform and relatively flat, with no noticeable pinholes or defects over 5 μm × 5 μm areas. The SC films are marginally smoother (see the rms roughness values in Table 1) than both LS P3HT and LS P3HT/Au NP films.

The thickness of LS P3HT films was 5.0 ± 1.3 and 5.5 ± 1.1 nm, as determined by TM-AFM height profile analysis of a mechanically made scratch and simulation of the X-ray specular reflectivity profile, respectively (data discussed below). These values are within the range expected for a single lamella-type bilayer of P3HT (with the *b*-axis parallel to the substrate plane, as depicted in Figure 2), based on previous XRD[46] and TM-AFM[70] measurements. Film thickness values for SC films
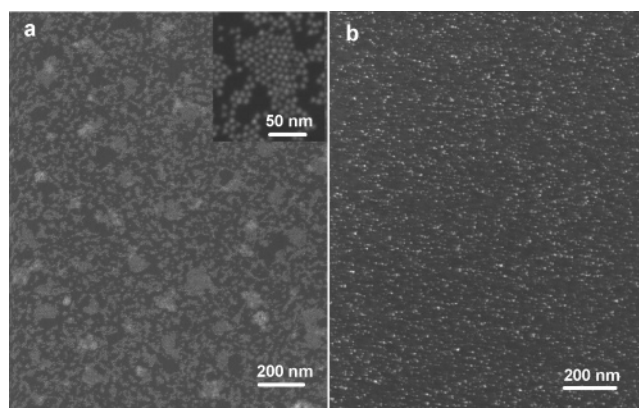

Figure 3. FE-SEM images of P3HT/Au NP SC (a) and LS (b) composite films. The inset in part a shows a higher magnification image of the SC composite films to illustrate NP hexagonal packing organization.

of 7.0 ± 1.2 and 7.6 ± 1.5 nm, as determined by TM-AFM and X-ray reflectivity, respectively, suggest a film comprised of three or four P3HT monolayers, again assuming the *b*-axis is parallel to the plane of the substrate. However, this assignment is not definitive, as previous studies have demonstrated crystalline regions in spin cast P3HT films where the thiophene rings can stand either parallel or normal to the substrate plane.[24,71] Thus, to ascertain unequivocally the arrangement of the polymer, XRD and X-ray reflectivity studies were performed (vide infra).

P3HT/Au NP Films. P3HT/Au NP LS and SC films were found to be 10 and 15 nm thick, respectively. The increase in thickness with Au NP addition is comparable with the dimension of an Au NP (core diameter 5.4 ± 0 3 nm). However, NPs can adopt various arrangements within the composite films, and in order to identify the film structure, FE-SEM and X-ray techniques were employed.

FE-SEM images, shown in Figure 3, were taken of the composite films to ascertain NP organization. Relatively low magnification images are shown to provide a more representative picture over an area comparable to that probed in the SECM experiments, reported later. There is a significant difference in NP distribution in the two films: NPs in the SC film arrange into hexagonally packed clusters (as shown in the higher magnification inset in Figure 3a), whereas NPs in the LS films are more or less homogeneously distributed and NP clustering is less pronounced. This difference is perhaps not unexpected given that the starting solution was an order of magnitude more concentrated for SC film preparation and film formation occurs over different time scales for the two preparative procedures.

Note that, since the thickness and hence the number of monolayers of P3HT present in the LS composite films is known, the surface density of Au NPs estimated from the FE-SEM images can be compared to the expected value. The NP densities were approximately 40% less than expected, indicating some loss of material to the subphase when fabricating LS films.

Film Molecular Organization. *XRD Measurements.* XRD measurements to determine P3HT film structure were performed on slightly thicker films (14 monolayer LS films and 5 mg mL^{-1} P3HT in chloroform for SC films) because of signal-to-noise considerations.[72] Structural organization, however, with respect to polymer backbone orientation, is likely to be comparable between the thin and slightly thicker films. To date, changes in the orientation of the crystalline domains in P3HT films have only been observed when very significant changes have been made in film thickness.[71]
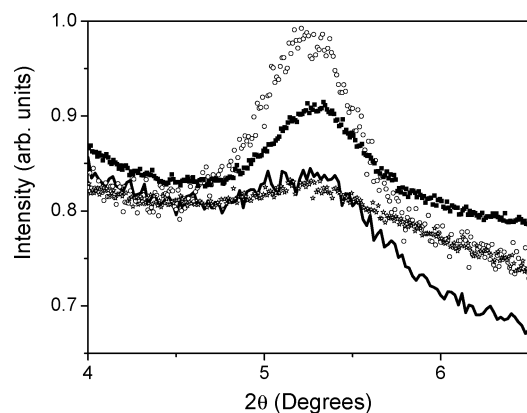
P3HT/Au NP Composite Films

J. Phys. Chem. B, Vol. 109, No. 41, 2005 **19339**

Figure 4. X-ray diffraction omega-2theta scans displayed in terms of 2θ (from top to bottom) for a 14 monolayer LS P3HT film (○), a 14 monolayer LS P3HT/Au NP film (■), a SC (5 mg mL^{-1}) P3HT/Au NP film (−), and a SC (5 mg mL^{-1}) P3HT film (☆). The background function is accounted for by the scattering of the glass substrate.

TABLE 2: Fitted 2θ Peak and d-Spacing Values (where $d = a$) for SC and LS P3HT and P3HT/Au NP (1:1) Films

sample	fitted 2θ peak (deg)	fitted d-spacing (Å)
SC P3HT	5.148 ± 0.008	16.95 ± 0.02
LS P3HT	5.222 ± 0.005	16.755 ± 0.006
SC (1:1)	5.450 ± 0.02	16.20 ± 0.06
LS (1:1)	5.272 ± 0.003	16.648 ± 0.004

Figure 4 shows XRD results for representative LS and SC films, with and without Au NPs. As seen in Figure 4, all films showed XRD first-order reflections at small 2θ angles, ~5°. Nonlinear curve fitting was used to obtain precise values for the 2θ peak position and corresponding interplanar spacing (Table 2). Assuming a rectangular unit cell,[73−75] the d-values of these first-order reflections are equivalent to the lattice parameter normal to the surface, and thus, distance a, as defined in Figure 2, is aligned normal to the sample surface and distance b (Figure 2) is the azimuthal parameter.[76] *XRD thus unambiguously corroborates the picture of molecular organization proposed in Figure 2.* This structural orientation, with interchain $\pi-\pi$ stacking in the same orientation as charge flow, is the most favorable for lateral charge transport which makes the results of this study relevant for OFET applications.[24]

The small angle reflections of 5.22 and 5.15° for P3HT LS and SC films, respectively, correspond to a lamella interchain spacing (distance denoted a in Figure 2) of 16.76 and 16.95 Å, respectively, comparable to values previously obtained for P3HT.[59,74] The only literature for a in a LS P3HT film

(determined with a multilayer LS film, spread from a 0.25 mg mL^{-1} chloroform solution) is 17.8 Å[46] which is significantly larger than the value we obtain, indicating a closer packed arrangement in the films described herein.

Surprisingly, both SC and LS composite P3HT/Au NP films showed a crystalline structure, exhibiting a 2θ peak at ~5.27 and ~5.45°, respectively (Figure 4 and Table 2), suggesting a structure for the polymer in the composite akin to that for the pure films. Inclusion of Au NPs does not appear to disrupt the supramolecular self-assembly of P3HT, and the corresponding distance a of lamella separation, 16.20 and 16.65 Å for SC and LS films, respectively, is within the range of previously reported values for pure films.[46,59,74] This result contrasts with a previous report of SC composite films of poly(3-octylthiophene) and nonprotected Au NPs with a mean diameter of 4 and 7 nm, where inclusion of Au NPs led to a loss of polymer order, as no low angle XRD peak was found.[40]

X-ray Specular Reflectometry. Specular reflectometry is a very sensitive technique for probing film thickness, roughness, and density variations perpendicular to the substrates. For example, it has been applied to study monolayers of regioregular P3ATs to distinguish between substituent nature and tilt.[73] In contrast to the XRD measurements, described above, ultrathin films can be employed. Reflectometry measurements for representative SC and LS P3HT films are shown in Figure 5. The profiles obtained were simulated, and excellent fits were achieved for both cases.

Reflectometry simulations are nonunique in the sense that a change in one parameter can be compensated for by subsequent changes throughout the structure. However, parameters were only allowed to vary within physically reasonable values, guided by the results of previous measurements of physical properties.[59,70,74,77] Thus, for example, the thicknesses for the SC and LS samples derived from simulation were necessarily in excellent agreement with the AFM measurements. The best fit for the spectrum of the LS film (Figure 5b) was achieved when a bilayer of P3HT was assumed. The model divided the polymer bilayer into seven layers (see Figure 6 and Table 3), corresponding to the upper (and lower) hexyl chains (L_{hex}), the two thiophene backbones (L_{thio}), and the center hexyl chains. It was found that the model improved significantly when a denser center region (with respect to L_{hex}) was included in the simulation. This layer was included and assigned to a region in which the hexyl chains were interdigitated. Consequently, the hexyl chains in the center of the bilayer comprised of three layers: a top (and bottom) layer corresponding to the portion
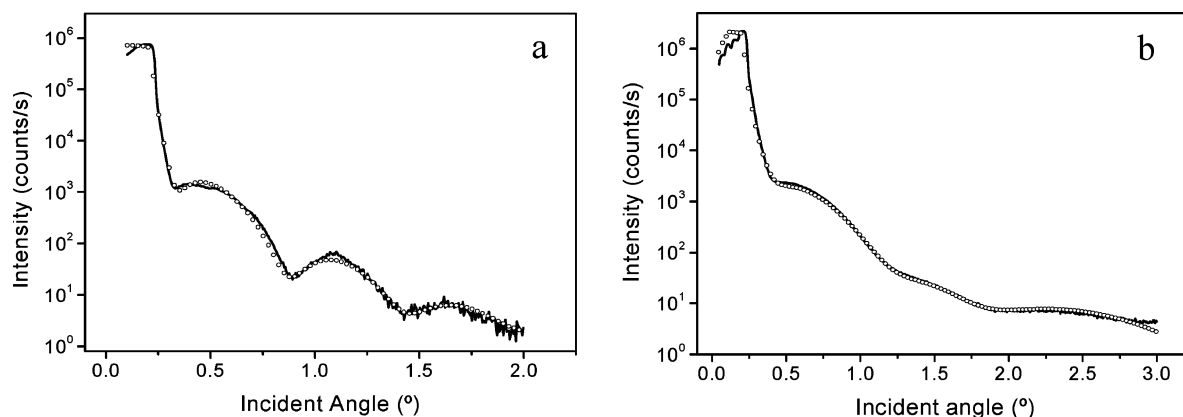

Figure 5. Measured (−) and fitted (○) X-ray reflectivity profiles for P3HT SC (a) and LS (b) films. Note that the LS simulations provide better agreement with the measured profiles than those for SC films indicating a more planar structure. The parameters could be varied within approximately 10−20% and still provide a reasonable fit to the experimental data.
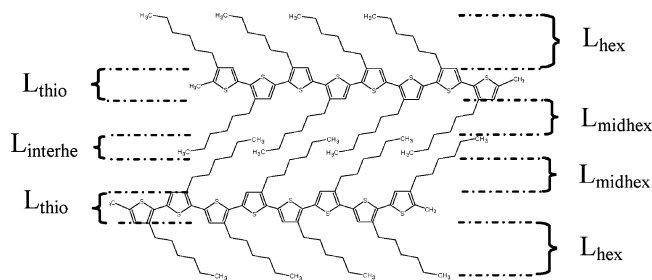
Figure 6. Schematic of the structure of LS P3HT films and X-ray reflectivity layer assignment.

TABLE 3: Summary of the X-ray Reflectivity Parameters for LS P3HT Films

layer	density (g cm^{-3})	thickness (nm)	roughness (nm)
glass	2.14	600000	0.12
L_{hex}	0.38	1.08	0.99
L_{thio}	1.11	0.85	0.65
L_{midhex}	0.25	0.51	0.05
$L_{interhex}$	0.84	0.47	1.02
L_{midhex}	0.35	0.60	0.90
L_{thio}	1.07	0.97	1.04
L_{hex}	0.61	1.08	0.88

TABLE 4: Summary of the X-ray Reflectivity Parameters for SC P3HT Films

layer	density (g cm^{-3})	thickness (nm)	roughness (nm)
glass	2.30	600000	0.13
L_{mono1}	0.99	2.53	0.39
L_{mono2}	1.03	2.63	0.73
L_{mono3}	0.95	2.50	0.68

of hexyl chains that were not interdigitated (L_{midhex}) and a denser middle region for the interdigitated part of the hexyl chains ($L_{interhex}$). The SC film was successfully simulated using three layers, assigned to three polymer monolayers: L_{mono1}, L_{mono2}, and L_{mono3} (Figure 5a and Table 4). The thickness of each layer was greater than what might be expected for a P3HT monolayer, indicating a rather loose structure.

X-ray reflectivity was an optimal technique for investigating NP distribution within the composite films, due to its sensitivity to electron (and hence mass) density variations perpendicular to film substrates. Figure 7 shows measured and modeled reflectivity profiles for representative samples of LS and SC composite films. In the case of the SC sample, a reasonable simulation could not be achieved by assuming a homogeneous,
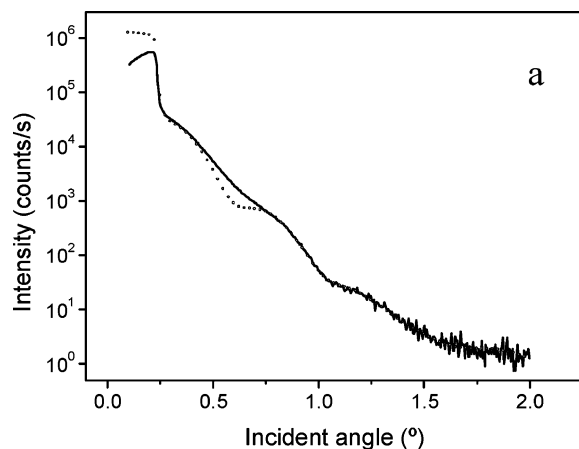
TABLE 5: Summary of the X-ray Reflectivity Parameters for SC P3HT/Au NP Films

layer	density (g cm^{-3})	thickness (nm)	roughness (nm)
glass	2.54	600000	0.58
$L_{1:1a}$	0.68	3.27	0.57
$L_{1:1b}$	1.18	3.41	0.05
$L_{1:1c}$	1.07	4.26	1.33

uniform layer of Au NPs within the structure. Instead, the best fit (Figure 7a and Table 5) was obtained by slightly increasing the average density of the whole structure and increasing the total thickness of the polymer monolayers (thus accounting, respectively, for the change in the measured profile around the critical angle and the change in fringe spacing). Although this indicates the presence of some denser material, compared with the pure P3HT SC sample, there was no apparent preferential location for the NPs within the film, at least within the limits of the simulation using laterally uniform layers.

In contrast, the LS film profile (Figure 7b) could be modeled assuming a distinct denser (Au NP) layer. Different layer arrangements were investigated, including separating the Au NP into several layers, and the closest fit was obtained when a uniform Au NP layer (L_{AuNP}) was positioned between four less dense organic layers (Figure 8 and Table 6). Inspection of layer
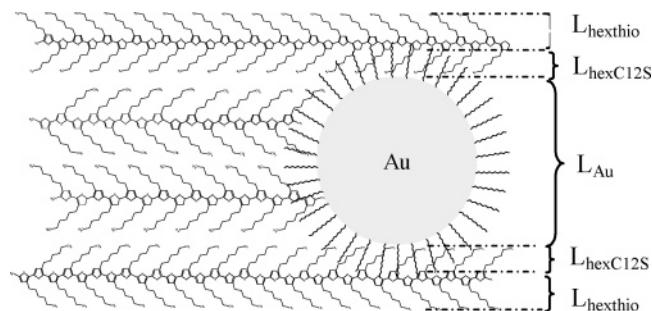

Figure 8. Schematic (not to scale) of the structure of LS P3HT/Au NP films and X-ray reflectivity layer assignment. The interaction between the NP dodecanethiolate chains and the polymer is simplified and is for illustration purposes only. Note that the reflectivity simulation model necessitates a denser middle region, most likely where the majority of Au NPs are located, but cannot distinguish between a middle region comprised of just Au NP or of Au NP and P3HT strands.

thickness, density, and roughness parameters allowed assignment of the organic layers to an upper (and lower) layer, correspond-
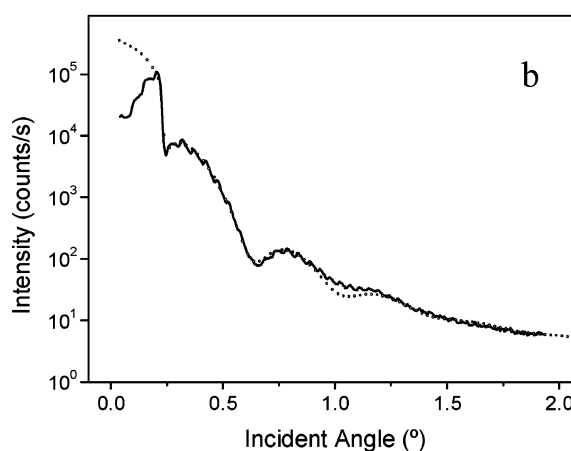

Figure 7. Measured (—) and fitted (○) X-ray reflectivity profiles for 1:1 P3HT/Au NP SC (a) and LS (b) films. The SC composite proved impossible to simulate by integrating the NP into the structure as planar layers; rather, the average density and thickness were increased in an attempt to account for the presence of NPs. The LS composite was modeled with a preferred orientation of NPs between the polymer bilayer. The ripple on the LS profile (b) is from the instrument function and should be ignored. The parameters could be varied within approximately 10−20% and still provide a reasonable fit to the experimental data.
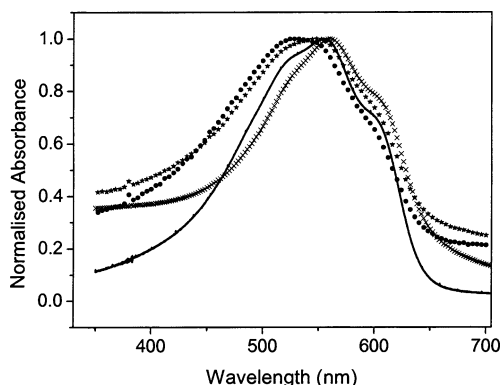
P3HT/Au NP Composite Films

J. Phys. Chem. B, Vol. 109, No. 41, 2005 **19341**

Figure 9. Normalized UV−visible absorption spectra for (from top to bottom at 700 nm) LS P3HT/Au NP (★), LS P3HT (●), SC P3HT/Au NP (×), and SC P3HT (−) films.

TABLE 6: Summary of the X-ray Reflectivity Parameters for LS P3HT/Au NP Films

layer	density (g cm^{-3})	thickness (nm)	roughness (nm)
glass	2.51	600000	0.10
L$_{hexthio}$	0.81	1.65	0.04
L$_{hexC12S}$	1.01	0.95	2.19
L$_{AuNP}$	2.02	6.18	2.27
L$_{hexC12S}$	0.55	0.88	2.28
L$_{hexthio}$	0.81	1.02	0.93

ing to the hexyl chains and the thiophene backbone (L$_{hexthio}$), and a layer adjacent to the Au NPs, corresponding to the interpenetrating hexyl and dodecanethiolate (L$_{hexC12S}$) chains. The density for the middle layer (L$_{AuNP}$) was a significant parameter when differentiating between candidate models, and the assumed value (2.0 g cm^{-3}) was comparable to the expected density for a single layered Au NP disposition, as estimated from the LS FE-SEM image (Figure 3b). Note that the reflectrometry model could not differentiate between a middle layer comprised solely of Au NPs or of P3HT strands and Au NPs. Consequently, the structure depicted in the schematic in Figure 8 should be taken as a likely, but not absolute, arrangement.

The results of UV−visible absorption spectroscopy on these films are shown in Figure 9, with the wavelength peak maximum (λ_{max}) values summarized in Table 1. Note that the oval spot size for the absorption measurement was 0.6 × 0.9 mm^2 and the results thus reflect the average organization over that area. There is a clear red shift (∼16−19 nm) in λ_{max} in SC films compared with LS films, indicating a lower energy $\pi-\pi^*$ transition and thus a longer delocalization of the exciton wave function (i.e., a longer effective conjugation length) in the P3HT SC film. The shift in λ_{max} in the SC P3HT/Au NP film, however, cannot be directly attributed to structural changes in the polymer, as NPs in the solid state exhibit a broad absorption spectrum with a λ_{max} peak centered at 560 nm.[62] In contrast, a shoulder at lower energies (∼600 nm) is more evident in the SC spectra. This subgap feature is due solely to the polymer, and although conventionally attributed to the 0−0 vibronic origin of intrachain excitons, it has recently been reassigned and is now thought to be due to an interchain process.[26] Therefore, the level of interchain order is related to the intensity of this lower energy feature in the spectrum[25,26] and the results obtained indicate that SC films are more ordered than their LS counterparts.

Lateral Film Conductivity. Lateral conductivity in P3HT and P3HT/Au NP films, with the polymer in its unintentionally doped state, was investigated by SECM steady-state feedback mode approach curves.[78] Figure 10 shows a schematic of the experimental arrangement. In a typical experiment, a small
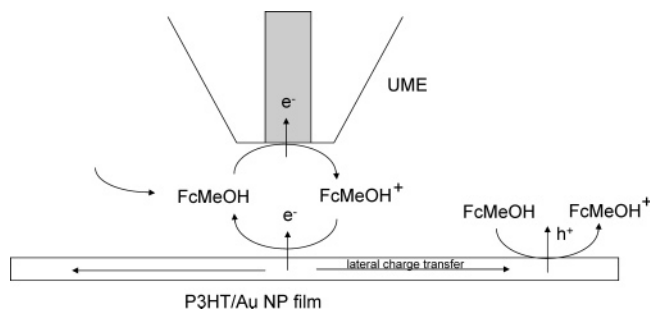

Figure 10. Schematic of the SECM setup for measuring the lateral conductivity of LS and SC films. Note that the film is on a (inert) solid support.

volume of the redox mediator (FcMeOH), ∼20 μL, was placed on the glass substrate supporting the P3HT film. Both the Pt UME and the Ag/AgCl reference electrode were immersed in the solution droplet. The UME was held at a potential where oxidation of FcMeOH to FcMeOH$^+$ occurred at a diffusion-limited rate (+0.3 V vs Ag/AgCl), and the current at the tip was measured as the tip was brought close to the substrate. It should be emphasized that FcMeOH$^+$ electrogenerated at the UME is not sufficiently oxidizing to chemically oxidize P3HT.[79] Rather, FcMeOH$^+$ injects holes into the valence band on P3HT and the measured feedback response arises from the native conductivity intrinsic of P3HT in its unintentionally doped state.

The tip current is affected by two processes:[80] the hindrance of FcMeOH diffusion to the UME while approaching the film (which causes a decrease in the current) and the regeneration of FcMeOH by the film (which causes an increase in the measured current). The regeneration of the electroactive species is driven by lateral conductivity within the film and the kinetics of the redox process.[51,54] The relative contribution of the lateral conductivity to the tip current tends to dominate as the relative contribution of hindered diffusion is decreased, effected by reducing mediator concentration. Thus, from the concentration dependence of the observed feedback response, the lateral conductivity of a film can be evaluated.[52,54]

Figure 11 shows examples of experimental SECM approach curves to P3HT and P3HT/Au NP SC and LS films deposited on glass. The current and distance have been normalized by the steady-state limiting current far from the substrate (i_∞) and by the UME radius (r), respectively. For all sets of approach curve data shown in Figure 11, the concentration of the redox mediator decreases from the bottom to the top. The lowest curve (solid line) in each of the four plots is the theoretical approach curve to an inert (insulating) substrate. Note that, for the SC films, as the bulk solution mediator concentration is decreased, the contribution of film lateral conductivity to the feedback response becomes apparent at much higher concentrations (3.3 and 3.0 mM for P3HT and P3HT/Au NP, respectively) than for the LS films (170 and 190 μM for P3HT and P3HT/Au NP, respectively). This indicates that the conductivity of SC films is considerably higher than that of LS films.

Alongside the experimental data, Figure 11 also shows the corresponding fits to theory, obtained with a model described in detail elsewhere.[51] Essentially, the model assumes that the conduction current is directly proportional to the local electrochemical potential gradient set by the concentration ratio of the redox couple in solution. The transport process in the film is described by the following equation:

$$\frac{\partial^2 \tilde{\mu}}{\partial R^2} + \frac{1}{R}\frac{\partial \tilde{\mu}}{\partial R} - \frac{K^0}{\Sigma}((1-C)e^{\tilde{\mu}/2} - Ce^{\tilde{\mu}/2}) = 0 \qquad (1)$$
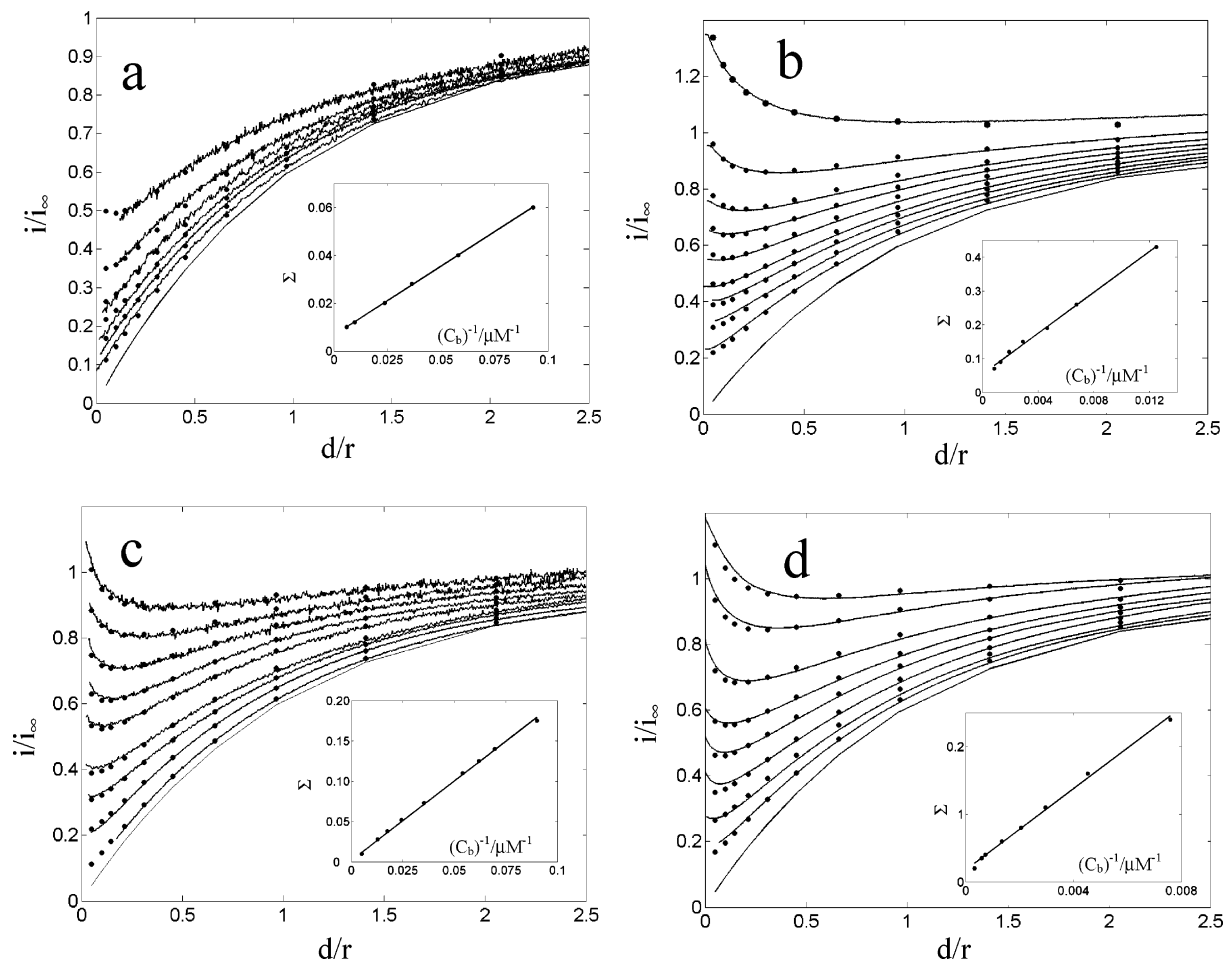
Figure 11. Experimental approach curves (solid lines) and corresponding fits to theory (dots), where the normalized tip current (i/i_∞) is plotted versus the normalized tip−substrate separation (d/r) for (a) P3HT LS film (concentration of redox mediator 170, 150, 100, 45, 17, and 10 μM (from bottom to top)), (b) P3HT SC film (concentration of redox mediator 3300, 1700, 1170, 770, 520, 340, 210, 150, and 80 μM (from bottom to top)), (c) P3HT/AuNP LS film (concentration of redox mediator 190, 80, 60, 40, 30, 20, 16, 14, and 10 μM (from bottom to top)), and (d) P3HT/Au NP SC film (concentration of redox mediator 3000, 1700, 1400, 700, 500, 300, 200, and 130 μM (from bottom to top)). The insets show the normalized conductivity (Σ) as a function of the inverse of the solution redox mediator concentration (c^b). The lowest curve in each graph is the theoretical response for the approach to an insulator.

where $R = d/r$ and $\tilde{\mu} = (\mu - \mu^0)/kT$ is the dimensionless electrochemical potential of the electrons in the film, k is Boltzmann's constant, and T is the absolute temperature. The dimensionless standard rate constant of the electron transfer (ET) reaction between the solution redox couple and the film is defined by $K^0 = k^0 r/D$, where D is the diffusion coefficient of the solution redox couple (7.0×10^{-6} cm^2 s^{-1}). C is the dimensionless concentration of the solution redox couple at the film ($C = c_{Red}/c^b$, where c_{Red} and c^b are the concentration of the reduced form of the redox couple at the film and the total concentration of mediator in the bulk, respectively), and Σ is the dimensionless conductivity in the film given by the following equation:

$$\Sigma = \frac{\sigma kT \Delta z}{e^2 r D c^b N_A} \quad (2)$$

Here, σ is the film conductivity, e is the elementary charge, and N_A is Avogadro's constant.

All experimental approach curves for both types of films were fitted with a relatively high value of the ET rate constant ($K^0 = 10$, corresponding to $k^0 = 5.6 \times 10^{-2}$ cm s^{-1}), which is expected given the reversibility of the mediator couple used. The value of the equilibrium electrochemical potential of the film (μ_{eq}) used to fit the feedback response was 2.9. This

parameter is set by the concentration ratio of the two forms of the redox couple in bulk solution (c^b_{Red}/c^b_{Ox}), which, for the case of FcMeOH, was found to be 0.95.[51] To fit the data in Figure 11, families of approach curves were simulated,[81] keeping the above-mentioned values of K^0 and μ_{eq} constant (for a particular film) and varying the normalized conductivity (Σ). The insets of Figure 11 demonstrate the linear dependence of Σ on the inverse of c^b, as suggested by eq 2, from which conductivity values (σ/S cm^{-1}) were calculated (Table 1).

Relationship between Film Structure and Conductivity. Since a comparable supramolecular orientation was found for both LS and SC P3HT films, the large difference ($\sim$26 times) in lateral conductivity of the two types of film cannot be attributed to the distinct charge transport anisotropy ($\sim$100) known for P3HT.[24,82] The measured difference in conductivity of the two types of film arises from two factors: thickness and molecular order.

Variable-range hopping lengths in P3HT have been estimated to be relatively large ($\sim$20 nm for undoped P3HT films),[31] and thus, as film thickness increases and becomes comparable to the hopping distance, a dimensionality transition from 2D to 3D is expected.[83,84] In these ultrathin films, lateral charge transport is inhibited by charge percolation between ordered domains within the film,[70] and consequently, a small increase in film thickness facilitates charge transport across defects,

P3HT/Au NP Composite Films

J. Phys. Chem. B, Vol. 109, No. 41, 2005 **19343**

vacancies, and grain boundaries. Clearly, the difference in thickness between SC films (three monolayers) and LS films (two monolayers) is at least partly responsible for the conductivity difference between the two.

Macroscopic lateral conductivity in P3HT is governed by interchain charge transport. We have shown that SC films are more compact, have longer effective conjugation lengths, and have a higher degree of interchain order; all are factors which provide an explanation for the conductivity found in SC films.

In composite films, NPs (or clusters of NPs) are not sufficiently close (Figure 3) for interparticle charge transport to occur over a long range. Moreover, P3HT is preferentially a p-type semiconductor,[85] and thus Au NPs (which are likely to be negatively charged)[86] will not dope the polymer, at least not in the conventional sense. The observed lateral conductivity in the composites will be determined by variable-range hopping within P3HT. The addition of NPs to SC films led to a marginal decrease in lateral conductivity (compared to the native film), whereas inclusion of NPs into LS films increased the lateral conductivity values by a factor of 2. The latter effect is almost certainly a consequence of the increased thickness of the LS composite films compared to the pure LS films. Note, however, that SC composite films still exhibited by far the highest conductivity due to the higher degree of structural ordering in these films.

Conclusions

In summary, the present study has provided the first detailed comparison of the structural and electrical properties of spin cast and Langmuir−Schaeffer films of a π-conjugated polymer (P3HT). By careful control over the preparation conditions and the composite component ratio, ultrathin, uniform, and relatively flat P3HT and P3HT/Au NP films have been fabricated by spin casting and the Langmuir−Schaeffer technique. The supramolecular orientation of the polymer in the ultrathin P3HT LS and SC films exhibited the preferred orientation for high lateral carrier mobility (Figure 2). Uniform SC and LS P3HT/Au NP composite films could be made by the incorporation of 50 wt % highly monodispersed Au NPs. Significantly, inclusion of Au NPs into both LS and SC P3HT films did not perturb the long-range crystalline structure of the polymer (as determined by XRD). However, as shown by FE-SEM, the NP organization and arrangement within the LS and SC composites varied significantly.

SECM has been shown to be an effective and sensitive probe of lateral conductivity for both pure P3HT films and composites. Together with the structural data obtained, the studies herein have demonstrated how structural organization impacts lateral conductivity. The extension of the SECM technique to other systems is envisaged.

References and Notes

(1) Markovich, G.; Collier, C. P.; Henrichs, S. E.; Remacle, F.; Levine, R. D.; Heath, J. R. *Acc. Chem. Res.* **1999**, *32*, 415.

(2) Shenhar, R.; Rotello, V. M. *Acc. Chem. Res.* **2003**, *36*, 549.

(3) Templeton, A. C.; Wuelfing, W. P.; Murray, R. W. *Acc. Chem. Res.* **2000**, *33*, 27.

(4) Schmid, G. *Nanoparticles*; Wiley-VCH: Weinheim, Germany, 2004.

(5) Klabunde, K. J. *Nanoscale Materials in Chemistry*; Wiley-Interscience: New York, 2001.

(6) Feldheim, D. L.; Foss, C. A., Jr. *Metal Nanoparticles*; Marcel Dekker: New York, 2002.

(7) Fendler, J. H. *Nanoparticles and Nanostructured Films: Preparation, Characterization and Applications*; Wiley-VCH: Weinheim, Germany, 1998.

(8) Daniel, M.-C.; Astruc, D. *Chem. Rev.* **2004**, *104*, 293.

(9) Boal, A. K.; Ilhan, F.; DeRouchey, J. E.; Thurn-Albrecht, T.; Russell, T. P.; Rotello, V. M. *Nature* **2000**, *404*, 746.

(10) Hicks, J. F.; Young, S.-S.; Murray, R. W. *Langmuir* **2002**, *18*, 2288.

(11) Wuelfing, W. P.; Murray, R. W. *J. Phys. Chem. B* **2002**, *106*, 3139.

(12) Gangopadhyay, R.; De, A. *Chem. Mater.* **2000**, *12*, 608 and references therein.

(13) Reuter, T.; Vidoni, O.; Torma, V.; Schmid, G.; Nan, L.; Gleiche, M.; Chi, L.; Fuchs, H. *Nano Lett.* **2002**, *2* (7), 709.

(14) Croissant, M. J.; Napporn, T.; Léger, J.-M.; Lamy, C. *Electrochim. Acta* **1998**, *43*, 2447.

(15) Coutanceau, C.; Croissant, M. J.; Napporn, T.; Lamy, C. *Electrochim. Acta* **2000**, *46*, 579.

(16) Kessler, T.; Castro Luna, A. M. *J. Appl. Electrochem.* **2002**, *32*, 825.

(17) Kim, J.-H.; Cho, J. H.; Cha, G. S.; Lee, C. W.; Kim, H. B.; Paek, S. H. *Biosens. Bioelectron.* **2000**, *14*, 907.

(18) Matsui, J.; Akamatsu, K.; Nishiguchi, S.; Miyoshi, D.; Nawafune, H.; Tamaki, K.; Sugimoto, N. *Anal. Chem.* **2004**, *76*, 1310.

(19) Hu, C. C.; Chen, E.; Lin, J. Y. *Electrochim. Acta* **2002**, *47*, 2741.

(20) Malik, M. A.; Galkowski, M. T.; Bala, H.; Grzybowska, B.; Kulesza, J. *Electrochim. Acta* **1999**, *44*, 2157.

(21) Zhai, L.; McCullough, R. D. *J. Mater. Chem.* **2004**, *14*, 141.

(22) Babel, A.; Jenekhe, S. A. *Synth. Met.* **2005**, *148*, 169.

(23) Chang, J.-F.; Sun, B.; Breiby, D. W.; Nielsen, M. N.; Solling, T. I.; Giles, M.; McCulloch, I.; Sirringhaus, H. *Chem. Mater.* **2004**, *16*, 4772.

(24) Sirringhaus, H.; Brown, P. J.; Friend, R. H.; Nielsen M. M.; Bechgaard, K.; Langeveld-Voss, B. M. W.; Spiering A. J. H.; Janssen, R. A. J.; Meijer, E. W.; Herwig, P.; de Leeuw, D. M. *Nature* **1999**, *401*, 685.

(25) Brown, P. J.; Sirringhaus, H.; Harrison, M.; Shkunov, M.; Friend, R. H. *Phys. Rev. B* **2001**, *63*, 125204.

(26) Brown, P. J.; Thomas, D. A.; Wils, S.; Köhler, on, J. S.; Kim, J. S.; Ramsdale, C. M.; Sirringhaus, H.; Friend, R. H. *Phys. Rev. B* **2003**, *67*, 064203-1.

(27) Sheng, P. *Phys. Rev. B* **1980**, *21* (6), 2180.

(28) Li, Q.; Cruz, L.; Phillips, P. *Phys. Rev. B* **1993**, *47* (4), 1840.

(29) Andrade, J. S., Jr.; Shibusa, Y.; Arai Y.; Siqueira, A. F. *Synth. Met.* **1995**, *68*, 167.

(30) Mott, N. F.; Davis, E. A. *Electronic Processes in Non-Crystalline Materials*; Clarendon: Oxford, U.K., 1979; Chapters 2 and 3.

(31) Punkka, E.; Rubner, M. F.; Hettinger, J. D.; Brooks, J. S.; Hannahs, S. T. *Phys. Rev. B* **1991**, *43*, 9077.

(32) Yoon, C. O.; Reghu, M.; Moses, D.; Heeger, A. J.; Cao, Y.; Chen, T.-A.; Wu, X.; Reike, R. D. *Synth. Met.* **1995**, *75*, 229.

(33) Breimer, M. A.; Yevgeny, G.; Sheldon, S.; Sadik, O. A. *Nano Lett.* **2001**, *1*, 305.

(34) Wang, J.; Neoh, K. G.; Kang, E. T. *J. Colloid Interface Sci.* **2001**, *239*, 78.

(35) Sarma, T. K.; Chowdhury, D.; Paul, A.; Chattopadhyay, A. *Chem. Commun.* **2002**, *10*, 1048.

(36) Zhou, Y.; Itoh, H.; Uemura, T.; Naka, K.; Chujo, Y. *Chem. Commun.* **2001**, *7*, 613.

(37) O'Mullane, A.; Dale, S. E.; Macpherson, J. V.; Unwin P. R. *Chem. Commun.* **2004**, *14*, 1606.

(38) Hata, K.; Fujihara, H. *Chem. Commun.* **2002**, 2714.

(39) Peng, Z.; Wang, E.; Dong, S. *Electrochem. Commun.* **2002**, *4*, 210.

(40) Sarathy, K. V.; Narayan, K. S.; Kim, J.; White, J. O. *Chem. Phys. Lett.* **2000**, *318*, 543.

(41) Fell, H. J.; Samuelsen, E. J.; Als-Nielsen, J.; Grübel, G.; Mårdalen, J. *Solid State Commun.* **1995**, *94*, 843.

(42) Pal, A. J.; Ostergard, T.; Paloheimo, J.; Stubb, H. *App. Phys. Lett.* **1996**, *69*, 8.

(43) Watanabe, I.; Hong, K.; Rubner, M. F. *Langmuir* **1990**, *6*, 1164. Rikukawa, M.; Rubner, M. F. *Synth. Met.* **1992**, *47*, 203.

(44) Ochiai, K.; Rikukawa, M.; Sanui, K. *Chem. Commun.* **1999**, 867.

(45) Bjornholm, T.; Greve, D. R.; Reitzel, N.; Hassenkam, T.; Kjaer, K.; Howes, P. B.; Larsen, N. B.; Bogelund, J.; Jayaraman, M.; Ewbank, P. C.; McCullough, R. D. *J. Am. Chem. Soc.* **1998**, *120*, 7643.

(46) Xu, G.; Bao, Z.; Groves, J. T. *Langmuir* **2000**, *16*, 1834.

(47) Fichou, D. *Handbook of Oligo- and Polythiophenes*; Wiley-VCH: Weinheim, Germany, 1995.

(48) Horowitz, G.; Hajlaoui, R.; Bourguiga, R.; Hajlaoui, M. *Synth. Met.* **1999**, *101*, 401. Ziemelis, K. E.; Hussain, A. T.; Bradley, D. D. C.; Friend, R. H.; Ruhe, J.; Wegner, G. *Phys. Rev. Lett.* **1991**, *66*, 2231.

(49) Quinn, B. M.; Prieto, I.; Haram, S. K.; Bard, A. J. *J. Phys. Chem. B* **2001**, *105*, 7474.

(50) Liljeroth, P.; Quinn, B. M.; Ruiz, V.; Kontturi, K. *Chem. Commun.* **2003**, 1570.

(51) Liljeroth, P.; Vanmaekelbergh, D.; Ruiz, V.; Kontturi, K.; Jiang, H.; Kauppinen, E.; Quinn, B. M. *J. Am. Chem. Soc.* **2004**, *126* (22), 7126.

(52) Ruiz, V.; Liljeroth, P.; Quinn, B. M.; Kontturi, K. *Nano Lett.* **2003**, *3* (10), 1459.

(53) Mandler, D.; Unwin, P. R. *J. Phys. Chem. B* **2003**, *107*, 407.

(54) Zhang, J.; Barker, A. L.; Mandler, D.; Unwin, P. R. *J. Am. Chem. Soc.* **2003**, *125*, 9312.

(55) O'Mullane, A. P.; Macpherson, J. V.; Unwin, P. R.; Cervera-Montesinos, J.; Manzanares, J. A.; Frehill, F.; Vos, J. G. *J. Phys. Chem. B* **2004**, *108*, 7219.

(56) Slevin, C. J.; Unwin, P. R. *J. Am. Chem. Soc.* **2000**, *122*, 2597.

(57) Zhang, J.; Unwin, P. R. *J. Am. Chem. Soc.* **2002**, *124*, 2379.

(58) Zhang, J.; Slevin, C. J.; Morton, C.; Scott, P.; Walton, D. J.; Unwin, P. R. *J. Phys. Chem. B* **2001**, *105*, 11120.

(59) Chen, T.-A.; Wu, X.; Rieke, R. D. *J. Am. Chem. Soc.* **1995**, *117*, 233.

(60) Brust, M.; Walker, M.; Bethell, D.; Schiffrin, D. J.; Whyman, R. *Chem. Commun.* **1994**, *7*, 801.

(61) Shimizu, T.; Teranishi, T.; Hasegawa, S.; Miyake, M. *J. Phys. Chem. B* **2003**, *107*, 2719.

(62) Nicholson, P. G.; Ruiz, V.; Macpherson, J. V.; Unwin, P. R. *Chem. Commun.* **2005**, 1052.

(63) Fewster, P. F. *X-ray Scattering from Semiconductors*, 2nd ed.; Imperial College Press: 2003; Chapter 4.

(64) Bowen, D. K.; Tanner, B. K. *High-Resolution X-ray Diffraction and Topography*; Taylor & Francis Ltd: 1998.

(65) Als-Nielsen, J.; McMorrow, D. *Elements of Modern X-ray Physics*; John Wiley & Sons: 2001.

(66) Van Der Lee, A. *Solid State Sci.* **2000**, *2*, 257.

(67) Amphlett, J. L.; Denuault, G. *J. Phys. Chem. B* **1998**, *102*, 9946.

(68) Yang, S.; Fan, L.; Yang, S. *J. Phys. Chem. B* **2004**, *108*, 4394.

(69) Wegner, G. *Thin Solid Films* **1992**, *216*, 105.

(70) Sandberg, H. G. O.; Frey, G. L.; Shkunov, M. N.; Sirringhaus, H.; Friend, R.; Nielsen, M. M.; Kumpf, C. *Langmuir* **2002**, *18*, 10176.

(71) Fell, H. J.; Samuelsen, E. J.; Als-Nielsen, J.; Grubel, G.; Mardalen, J. *Solid State Commun.* **1995**, *94* (10), 843.

(72) Consequently, the only differences in the diffraction peaks that are significant to this study are the 2θ positions, as the other properties (for example, the full width at half-maximum or peak intensity) will vary as a direct result of the growth process.

(73) Reitzel, N.; Greve, D. R.; Kjaer, K.; Howes, P. B.; Jayaraman, M.; Savoy, S.; McCullough, R. D.; McDevitt, J. T.; Bjørnholm, T. *J. Am. Chem. Soc.* **2000**, *122*, 5788.

(74) Prosa, T. J.; Winokur, M. J.; Moulton, J.; Smith, P.; Heeger, A. J. *Macromolecules* **1992**, *25*, 4364.

(75) McCullough, R. D.; Tristam-Nagle, S.; Williams, S. P.; Lowe, R. D.; Jayaraman, M. *J. Am. Chem. Soc.* **1993**, *115*, 4910.

(76) Limitations of the goniometer mean the second lattice parameter cannot be measured directly without access to an asymmetric reflection (dependent on two lattice parameters rather than one).

(77) Chen, J.; Ratera, I.; Ogletree, D. F.; Salmeron, M.; Murphy, A. R.; Frechet, J. M. J. *Langmuir* **2005**, *21*, 1080.

(78) Bard, A. J.; Mirkin, M. V. *Scanning Electrochemical Microscopy*; Marcel Dekker: New York, 2001.

(79) Roncali, J. *Chem. Rev.* **1992**, *92*, 711.

(80) Kwak, J.; Bard, A. J. *J. Electrochem. Soc.* **1991**, *138*, 468.

(81) The diffusion problem was solved with a commercial finite element method package (FEMLAB, Comsol Ab, Sweden) for various values of d/r. The finite element mesh was first refined adaptively with $\Sigma = 0$, and then, the full, nonlinear problem was solved with that mesh. The number of elements employed was ordinarily $\sim 5 \times 10^4$.

(82) Kaneto, K.; Yoshino, K.; Inuishi, Y. *Jpn. J. Appl. Phys.* **1982**, *21* (9), 567.

(83) Paloheimo, J.; Kuivalainen, P.; Stubb, H.; Vuorimaa, E.; Yli-Lahti, P. *Appl. Phys. Lett.* **1990**, *56* (12), 1157.

(84) Butcher, P. N.; Hayden, K. J.; McInnes, J. A. *Philos. Mag.* **1977**, *36* (1), 19.

(85) Glenis, S.; Horowitz, G.; Tourillon, G.; Garnier, F. *Thin Solid Films* **1984**, *111*, 93.

(86) Quinn, B. M.; Lijeroth, P.; Ruiz, V.; Laaksonen, T.; Kontturi, K. *J. Am. Chem. Soc.* **2003**, *125*, 6644.